

The quantitative measurement of magnetic moments from phase images of nanoparticles and nanostructures—I. Fundamentals

Marco Beleggia^{*}, Takeshi Kasama, Rafal E. Dunin-Borkowski

Center for Electron Nanoscopy, Technical University of Denmark, DK-2800 Kgs. Lyngby, Denmark

ARTICLE INFO

Keywords:

Electron holography
Phase shift
Magnetic nanoparticles
Magnetic moment

ABSTRACT

An approach that can be used to measure the magnetic moment of a magnetized nanoparticle or nanostructure from an electron-optical phase image is introduced. The measurement scheme is based on integration of the gradient of the measured phase image within a circular boundary that contains the structure of interest. The quantity obtained is found to be directly proportional to the magnetic moment of the particle, with a constant of proportionality that does not depend on the particle's shape or magnetization state. The measurement of magnetic moments from both simulated and experimental phase images is demonstrated, and strategies are presented that can be utilized to overcome sources of error associated with, for example, the presence of neighboring magnetic particles and the perturbation of the holographic reference wave.

© 2009 Elsevier B.V. All rights reserved.

1. Introduction

Measurements of electron-optical phase shifts in transmission electron microscope (TEM) images, using techniques that include off-axis electron holography [1,2] and approaches based on the transport of intensity equation [3,4], are increasingly used to record maps of the projected in-plane magnetic induction of magnetized nanocrystals [5,6], nanostructures [7–9], thin films and devices [10,11], often with sub-10-nm spatial resolution [12]. Such phase images can be used to obtain quantitative information about parameters such as the magnetization or coercivity of a region of interest as well as about magnetic interactions and transitions between single- and multi-domain magnetic states. A key parameter, whose determination from a phase image has not previously been addressed in depth, is the magnetic moment of a nanoparticle or nanostructure

$$\mathbf{m} = \iiint \mathbf{M}(\mathbf{r}) d^3\mathbf{r}, \quad (1)$$

where $\mathbf{M}(\mathbf{r})$ is the position-dependent magnetization of the structure and \mathbf{r} is a three-dimensional position vector. The conceptual and mathematical difficulty of measuring \mathbf{m} stems from the fact that a phase image does not provide direct information about the magnetization field $\mathbf{M}(\mathbf{r})$; instead, the phase shift is proportional to a projection of the in-plane components of the three-dimensional magnetic induction vector field $\mathbf{B}(\mathbf{r})$, both within and around the specimen. Approaches for

measuring \mathbf{m} based on integration of the phase gradient have previously been suggested [13,14], but neither justified nor derived rigorously.

Here, we show mathematically that the magnetic moment of a nanoparticle or nanostructure can be measured quantitatively from either a phase image or its gradient components. We show that the approach can be employed to study particles with an arbitrary shape and magnetization state, and that no assumptions are necessary to extract the information. We establish strategies that can be used to identify and overcome sources of error, and we demonstrate the measurement of magnetic moments from both simulated and experimental phase images.

Fig. 1 shows an example of a representative experimental electron hologram and a corresponding projected magnetic induction map (comprising contours generated from the magnetic contribution to the recorded phase shift) acquired from three closely spaced ferrimagnetic crystals of magnetite (Fe_3O_4). The induction map shown in Fig. 1 is discussed and analyzed in detail below.

2. Basic considerations

The approach that we describe in this paper is based on the fundamental expression for the magnetic contribution to the electron-optical phase shift (referred to as “magnetic phase”) recorded from a magnetized specimen, which, in the reference frame of the microscope, can be written in the form [12]

$$\varphi(\mathbf{r}_\perp) = -\frac{e}{\hbar} \int_{-\infty}^{+\infty} A_z(\mathbf{r}_\perp, z) dz, \quad (2)$$

^{*} Corresponding author.

E-mail address: mb@cen.dtu.dk (M. Beleggia).

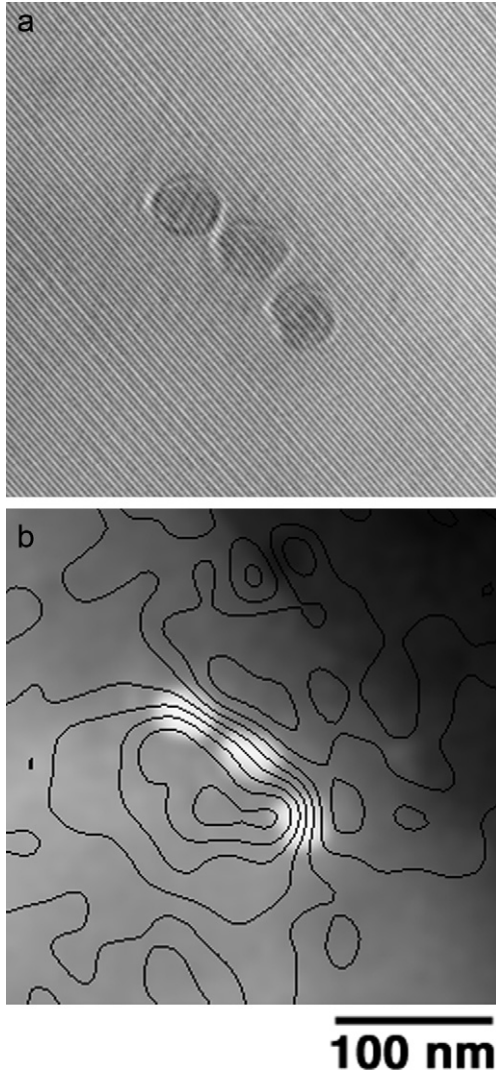


Fig. 1. (a) Off-axis electron hologram recorded at 300 kV in magnetic-field-free conditions from a chain of three approximately equidimensional ferrimagnetic magnetite nanocrystals supported on amorphous carbon. The crystals were extracted from a magnetotactic bacterium and deposited onto a holey carbon support film. The hologram was acquired using a Philips CM300 field emission gun TEM equipped with a Lorentz lens and an electrostatic biprism. (b) Corresponding magnetic induction map, formed by generating contours of spacing 0.0625 radians from the magnetic contribution to the recorded phase shift and superimposing them onto the mean inner potential contribution. The magnetic and mean inner potential contributions were determined by calculating half of the difference and half of the sum of phase images, between which the magnetization direction in the specimen had been reversed by applying a magnetic field to the specimen using the field of the conventional microscope objective lens.

where \mathbf{A} is the magnetic vector potential, the electron beam direction is along $-z$, and \mathbf{r}_\perp is a two-dimensional position vector in the object plane. The two orthogonal components of the magnetic phase gradient are

$$\partial_x \varphi(\mathbf{r}_\perp) = -\frac{e}{\hbar} \int_{-\infty}^{+\infty} \partial_x A_z(\mathbf{r}_\perp, z) dz \quad (3)$$

and

$$\partial_y \varphi(\mathbf{r}_\perp) = -\frac{e}{\hbar} \int_{-\infty}^{+\infty} \partial_y A_z(\mathbf{r}_\perp, z) dz. \quad (4)$$

As the relationship between \mathbf{B} and \mathbf{A}

$$\mathbf{B} = \nabla \times \mathbf{A}, \quad (5)$$

can be written explicitly as

$$B_x = \partial_y A_z - \partial_z A_y \quad (6)$$

and

$$B_y = -\partial_x A_z + \partial_z A_x, \quad (7)$$

Eqs. (3) and (4) can be rewritten in the forms

$$\begin{aligned} \frac{\hbar}{e} \partial_x \varphi(\mathbf{r}_\perp) &= \int_{-\infty}^{+\infty} B_y(\mathbf{r}_\perp, z) dz - \int_{-\infty}^{+\infty} \partial_z A_x(\mathbf{r}_\perp, z) dz \\ &= \int_{-\infty}^{+\infty} B_y(\mathbf{r}_\perp, z) dz - A_x(\mathbf{r}_\perp, z) \Big|_{z=-\infty}^{z=+\infty} \\ &= \int_{-\infty}^{+\infty} B_y(\mathbf{r}_\perp, z) dz \end{aligned} \quad (8)$$

and, similarly,

$$-\frac{\hbar}{e} \partial_y \varphi(\mathbf{r}_\perp) = \int_{-\infty}^{+\infty} B_x(\mathbf{r}_\perp, z) dz \quad (9)$$

due to the fact that any vector potential generated by finite magnetic sources must decay to zero at infinity. Eqs. (8) and (9) highlight the fact that the phase gradient component along a given direction is directly proportional to the magnetic induction component in the perpendicular direction, projected along the beam path. This relationship between the components of the phase gradient and the projected induction can be written in a single expression

$$\begin{aligned} \mathbf{B}_p(\mathbf{r}_\perp) &= \int_{-\infty}^{+\infty} \mathbf{B}(\mathbf{r}) dz = \frac{\hbar}{e} [-\partial_y \varphi(\mathbf{r}_\perp), \partial_x \varphi(\mathbf{r}_\perp)] \\ &= \frac{\hbar}{e} [\hat{\mathbf{z}} \times \nabla \varphi(\mathbf{r}_\perp)] \end{aligned} \quad (10)$$

and also forms the basis of proposals for magnetic vector field electron tomography [15,16].

Integration of the phase gradient would result in the expressions

$$\frac{\hbar}{e} \iint \partial_x \varphi(\mathbf{r}_\perp) d^2 \mathbf{r}_\perp = \iiint B_y(\mathbf{r}_\perp, z) d^2 \mathbf{r}_\perp dz = \iiint B_y(\mathbf{r}) d^3 \mathbf{r} \quad (11)$$

and

$$\begin{aligned} \frac{\hbar}{e} \iint \partial_y \varphi(\mathbf{r}_\perp) d^2 \mathbf{r}_\perp &= -\iiint B_x(\mathbf{r}_\perp, z) d^2 \mathbf{r}_\perp dz \\ &= -\iiint B_x(\mathbf{r}) d^3 \mathbf{r} \end{aligned} \quad (12)$$

in which the integrals are performed over some domains to be specified. Although the integrals in Eqs. (11) and (12) do not provide the “magnetic moment” as defined in Eq. (1) directly, their forms suggest that a relationship may exist between the quantities described in each of the expressions and the components of the desired moment \mathbf{m} . In this paper we show that such a relationship does exist, and we establish an approach for measuring \mathbf{m} experimentally. For convenience, the quantity

$$\mathbf{m}_B = \frac{1}{\mu_0} \iiint \mathbf{B}(\mathbf{r}) d^3 \mathbf{r} \quad (13)$$

will be referred to below as “inductive moment”. The inductive and magnetic moments have the same units (Am^2 or J/T in SI), and we choose to measure both quantities in multiples of Bohr magnetons $\mu_B = 9.274 \times 10^{-24} \text{ J/T}$.

3. Relationship between the inductive moment and the magnetic moment

From a practical perspective, it is interesting and important to notice that the volume integral of \mathbf{B} that defines \mathbf{m}_B in Eq. (13) is not absolutely convergent in a mathematical sense. This situation arises because \mathbf{B} is dipolar at large distances from a source, and so it decays with the third inverse power of r . For an integral carried out in three dimensions, this decay is not strong enough to guarantee *absolute* convergence, and Fubini's theorem (see, e.g., Section 4.5 in Ref. [17]) states that the result then depends on the order of integration. That is, if the integral in Eq. (13) is carried out along x and then y , then a different result may be obtained from that found by integrating along y and then x . Similarly, integration in spherical coordinates may provide a different answer from the use of Cartesian or cylindrical coordinates.

An analytical illustration of this mathematical anomaly is provided by considering a sphere that is magnetized uniformly along x with magnetization M , radius R , volume V and magnetic moment $\mathbf{m} = m\hat{\mathbf{x}} = MV\hat{\mathbf{x}}$, for which

$$\mathbf{B}(\mathbf{r}) = \frac{\mu_0 m}{4\pi} \left[\frac{3x\mathbf{r}}{r^5} - \frac{\hat{\mathbf{x}}}{r^3} \right] \quad \text{for } r > R,$$

$$\mathbf{B}(\mathbf{r}) = \frac{2}{3}\mu_0 M\hat{\mathbf{x}} \quad \text{for } r \leq R. \quad (14)$$

If the volume integral of $\mathbf{B}(\mathbf{r})$ is evaluated in a spherical region of radius $R_c > R$ centered on the sphere, then the inductive moment

$$\mathbf{m}_B = \frac{V}{\mu_0} \mathbf{B}(r \leq R) + \frac{m}{4\pi} \int_R^{R_c} r^2 dr \int_0^\pi \sin\theta d\theta \int_0^{2\pi} d\phi \left[\frac{3x\mathbf{r}}{r^5} - \frac{\hat{\mathbf{x}}}{r^3} \right] = \frac{2}{3} \mathbf{m} \quad (15)$$

because the second term vanishes when the angular integration is carried out. As demonstrated in Ref. [18], Eq. (5.62), the relationship between \mathbf{m}_B and \mathbf{m} in Eq. (15) remains valid for arbitrary shapes and magnetization states of the particle enclosed in the sphere of integration.

In contrast, if the flux Φ of \mathbf{B} is initially calculated in each plane perpendicular to the direction of the magnetic moment, then

$$\begin{aligned} \mathbf{m}_B &= \hat{\mathbf{x}} \int_{-\infty}^{+\infty} \Phi(x) dx = \hat{\mathbf{x}} \int_{-\infty}^{+\infty} dx \iint B_x(x, y, z) dx dy \\ &= \hat{\mathbf{x}} \int_{-\infty}^{+\infty} dx \left\{ \frac{2}{3} \pi M [R(x)]^2 + \frac{m}{4\pi} \int_{R(x)}^{+\infty} \rho d\rho \int_0^{2\pi} d\theta \left[\frac{2x^2 - \rho^2}{(x^2 + \rho^2)^{5/2}} \right] \right\} \\ &= \hat{\mathbf{x}} \int_{-\infty}^{+\infty} dx \left\{ \frac{2}{3} \pi M [R(x)]^2 - \frac{m}{2} \frac{[R(x)]^2}{(x^2 + [R(x)]^2)^{3/2}} \right\} \quad (16) \end{aligned}$$

$$= \hat{\mathbf{x}} \int_{-\infty}^{+\infty} dx \left\{ \frac{2}{3} \pi M [R(x)]^2 - \frac{1}{2} \frac{4\pi}{3} MR^3 \frac{[R(x)]^2}{R^3} \right\} = \mathbf{0}, \quad (17)$$

where $[R(x)]^2 = R^2 - x^2$ if $-R \leq x \leq R$ and 0 otherwise.

Although Eqs. (15) and (16) predict different values for the inductive moment of a uniformly magnetized sphere, they are both correct, and they each possess their own physical meaning. Confusingly, the experimental setup used in electron microscopy is still different. The signal is acquired as an integral along the beam direction, and the integral of \mathbf{B} in a spherical volume can never be measured directly. Moreover, the part of the object plane from which the phase can be retrieved is finite, and the region of integration can never be extended to include all of the return flux from the object. These restrictions suggest that an appropriate physical meaning for \mathbf{m}_B , in the context of electron microscopy, can be established by choosing a cylindrical coordinate system: the beam direction sets the axis of symmetry, while the finite field of view defines the perpendicular plane. Since the

quantities are integrated along the axis of symmetry, there is no need to specify the vertical position of the origin of the reference system.

The relationship between the inductive moment and the magnetic moment in cylindrical geometry is conveniently established by exploiting one form of Gauss' theorem (see Ref. [19]):

$$\begin{aligned} \mathbf{m}_B &= \frac{1}{\mu_0} \iiint_C \mathbf{B}(\mathbf{r}) d^3\mathbf{r} \\ &= \frac{1}{\mu_0} \iiint_C \nabla \times \mathbf{A}(\mathbf{r}) d^3\mathbf{r} = \frac{1}{\mu_0} \int_{\partial C} d\mathbf{S} \times \mathbf{A}(\mathbf{r}), \quad (18) \end{aligned}$$

where C denotes a cylinder that has radius R_c , infinite height and defines the region of integration, ∂C is its surface, and $d\mathbf{S}$ is a surface element directed along the outward normal ($\hat{\mathbf{r}}_\perp$ in this case). Since the top and bottom surfaces of C are at infinity, their contribution to the integral vanishes along with the vector potential, leaving

$$\mathbf{m}_B = \frac{R_c}{\mu_0} \int_{-\infty}^{+\infty} dz \int_0^{2\pi} d\theta \hat{\mathbf{r}}_\perp \times \mathbf{A}(R_c \cos\theta, R_c \sin\theta, z). \quad (19)$$

As the field generated by any magnetic structure can be thought of as a superposition of the fields generated by each elementary dipole comprising the particle (i.e., the magnetic moments of the material), we first determine the relationship between \mathbf{m}_B and \mathbf{m} for a point dipole that is oriented arbitrarily and displaced from the origin of the coordinate system. The vector potential of a dipole with moment $\mathbf{m} = [m_x, m_y, m_z]$ that is displaced from the origin by the vector $\mathbf{r}' = [r' \cos\theta', r' \sin\theta', z']$ (where, without loss of generality, $\theta' = 0$ is chosen to facilitate computation) is

$$\mathbf{A}(\mathbf{r}) = \frac{\mu_0}{4\pi} \frac{\mathbf{m} \times (\mathbf{r} - \mathbf{r}')}{|\mathbf{r} - \mathbf{r}'|^3}. \quad (20)$$

After evaluating the cross-product with \mathbf{r}_\perp and integrating along z ,

$$\mathbf{m}_B = \frac{R_c}{2\pi} \int_0^{2\pi} \frac{d\theta}{R_c^2 + r'^2 - 2R_c r' \cos\theta} \begin{bmatrix} \sin\theta(m_y r' - m_y R_c \cos\theta + m_x R_c \sin\theta) \\ -\cos\theta(m_y r' - m_y R_c \cos\theta + m_x R_c \sin\theta) \\ m_z(R_c - r' \cos\theta) \end{bmatrix}. \quad (21)$$

When all integrals are carried out explicitly with the condition $R_c > r'$ that reflects the elementary dipole being inside the cylinder, Eq. (21) reduces to

$$\mathbf{m}_B = \frac{1}{\mu_0} \iiint_C \mathbf{B}(\mathbf{r}) d^3\mathbf{r} = \left[\frac{1}{2} m_x, \frac{1}{2} m_y, m_z \right], \quad (22)$$

independent of the displacement of the dipole as well as the radius of integration. As the contribution from each elementary dipole in the structure can then be added, Eq. (22) remains valid for any shape and any magnetization state provided that the cylindrical region of integration is large enough to contain all of the magnetized matter.

Eq. (22) shows that the orientation of the three-dimensional vector \mathbf{m}_B is, in general, different from that of \mathbf{m} . For instance, $\mathbf{m} = m[1, 0, 1]$ corresponds to $\mathbf{m}_B = m[0.5, 0, 1]$. Significantly, however, in electron microscopy the vertical component of \mathbf{m}_B is generally lost, and only planar moments need to be considered. *Orientation in the plane is then preserved, and*

$$\mathbf{m}_B = \frac{1}{\mu_0} \iiint_C \mathbf{B}(\mathbf{r}) d^3\mathbf{r} = \frac{1}{2} \mathbf{m}. \quad (23)$$

For the remainder of this paper, we will consider only planar moments, i.e., $\mathbf{m} = [m_x, m_y]$ and $\mathbf{m}_B = [m_B^x, m_B^y]$ will be used to represent vectors with two components that lie only in the object plane, for which Eq. (23) holds.

When the cylinder of integration is external to the magnetized structure, i.e., $r' > R_c$, explicit integration of Eq. (21) results in

$$\mathbf{m}_B = \frac{1}{\mu_0} \iiint_C \mathbf{B}(\mathbf{r}) d^3\mathbf{r} = \frac{\pi R_c^2}{\mu_0} \mathbf{B}_p(\mathbf{0}), \quad (24)$$

where $\mathbf{B}_p(\mathbf{0})$ is the projected field of the external particle, as defined in Eq. (10) and evaluated at the center of the cylinder cross-section in the object plane. Eq. (24) is the equivalent of Eq. (5.63) in Ref. [18].

Referring back to Eq. (19), if the integration of the vector potential is carried out along z first, then the two planar components of the inductive moment can be related directly to the phase shift in the form

$$\mathbf{m}_B = \frac{\hbar R_c}{e\mu_0} \int_0^{2\pi} d\theta [-\sin\theta, \cos\theta] \varphi(R_c \cos\theta, R_c \sin\theta). \quad (25)$$

Eq. (25) suggests that there is an additional method for measuring the inductive moment: rather than integrating each of the phase gradient components, a loop-integral can be carried out on the magnetic phase shift directly. This alternative strategy can be used to bypass the numerical evaluation of the phase gradient.

Eqs. (22)–(24) provide a physically sound relationship between \mathbf{m}_B and \mathbf{m} . Together with Eqs. (11) and (12), or Eq. (25), they form the basis of the schemes that we propose below for measuring the magnetic moment \mathbf{m} from a phase image. Their application to simulated and experimental images is presented below.

4. Measurement of the magnetic moment

Having established the relationship between \mathbf{m}_B and \mathbf{m} , several practical issues associated with the measurement of the magnetic moment from experimental phase images can be addressed. Eqs. (11) and (12), together with the considerations discussed above, suggest that \mathbf{m}_B can be obtained simply by integrating two orthogonal components of the phase gradient in a circle that contains a magnetic structure of interest. Fig. 2 provides an illustrative example showing the simulated phase gradient components for four in-plane-magnetized non-overlapping identical disks, each of which has the same magnitude but a different orientation of \mathbf{m} . The ensemble of disks is representative of a generic magnetic structure with a non-uniform magnetization and a non-trivial shape. The total magnetic moment of this structure can be written in the form

$$\mathbf{m} = \sum_{i=1}^4 \mathbf{m}_i = m \sum_{i=1}^4 [\cos\theta_i, \sin\theta_i]. \quad (26)$$

The input values that were used to generate Fig. 2 correspond to

$$\mathbf{m} = m[1.349, 2.470] = 2.814m[\cos\theta_m, \sin\theta_m] \quad \text{with } \theta_m = 61.36^\circ. \quad (27)$$

By selecting an integration radius equal to half of the field of view, the two phase gradient components provide a measured inductive moment of

$$\mathbf{m}_B = m[0.6741, 1.234] = 1.406m[\cos\theta_m, \sin\theta_m] \quad \text{with } \theta_m = 61.30^\circ, \quad (28)$$

which, as expected, is half of the magnetic moment in Eq. (27), with the small differences in the fourth digit presumably resulting from the relatively small number of pixels (512 in each direction) employed in the simulation. The application of the alternative loop-integral procedure described in Eq. (25) to the four disks shown in Fig. 2, around the circumference shown in Fig. 2(b), provides exactly the same result as that obtained by integration of the phase gradient components.

The practical application of such a measurement scheme is, in general, complicated by the fact that different phase retrieval techniques are affected to different extents by unavoidable factors that introduce artifacts into recorded phase images, and therefore potentially into measurements of magnetic moments. We consider in detail below a number of potential sources of artifacts, and discuss opportunities for their identification and minimization.

4.1. Misalignment and changes in specimen morphology

The mean-inner potential, or electrostatic, contribution to the phase shift must typically be subtracted from a phase image to obtain the magnetic contribution that is used to measure the magnetic moment. This subtraction can be achieved by evaluating half of the difference between two aligned phase images that have been acquired before and after turning the specimen over. Alternative approaches include recording two phase images acquired either at different microscope accelerating voltages or before and after reversing the direction of magnetization in the specimen with external applied fields. Whichever approach is used, the effects of small (often sub-pixel) misalignment may be present in the difference image, especially at the edges of nanocrystals, where the specimen thickness varies rapidly.

These artifacts may result in an additional contribution to the magnetic phase, and in particular to the phase gradient. However, the measurement scheme proposed here appears to be robust against misalignment. If the measurement is carried out from a magnetic phase image that was obtained as described above, then the procedure is equivalent to measuring the moments of two identical particles, each carrying half the total moment, that are displaced slightly with respect to each other. Since the result of the measurement does not depend on shape or magnetization state, provided the integration circle is wide enough to contain the structure, the result will be exactly equal to the moment, independent of the amount and direction of misalignment. Furthermore, the measurement may in principle be carried out on the total phase image (electrostatic+magnetic), thereby avoiding the introduction of misalignment artifacts and errors associated with changes in the diffractivity condition of the structure of interest.

4.2. Low frequency phase artifacts

Spurious low spatial frequency artifacts may be present in a phase image, even if it is acquired using off-axis electron holography and if a vacuum reference hologram is recorded. These may arise from a number of factors that include, for example, movement of the biprism wire between the acquisition of sample and vacuum holograms. A linear slope added to the magnetic phase results in a perturbation to the integrated phase gradient, and hence to the magnetic moment, that depends quadratically on the integration radius. If the phase slope is $\mathbf{k} \cdot \mathbf{r}$, then the error is

$$\Delta \mathbf{m}_B = \frac{\pi \hbar}{e\mu_0} R_c^2 (\hat{\mathbf{z}} \times \mathbf{k}). \quad (29)$$

For a nanocrystal of radius $R = 50$ nm magnetized so that its inductive moment is 2.25×10^7 Bohr magnetons (corresponding to an average magnetization of 1 T), a linear term of 1 mrad/nm in the phase image results in an error in the magnetic moment measurement carried out over a circle of radius $R_c = 120$ nm of approximately 2.5×10^6 Bohr magnetons, or $\sim 10\%$. The smallest possible error is obtained when the radius of integration is equal

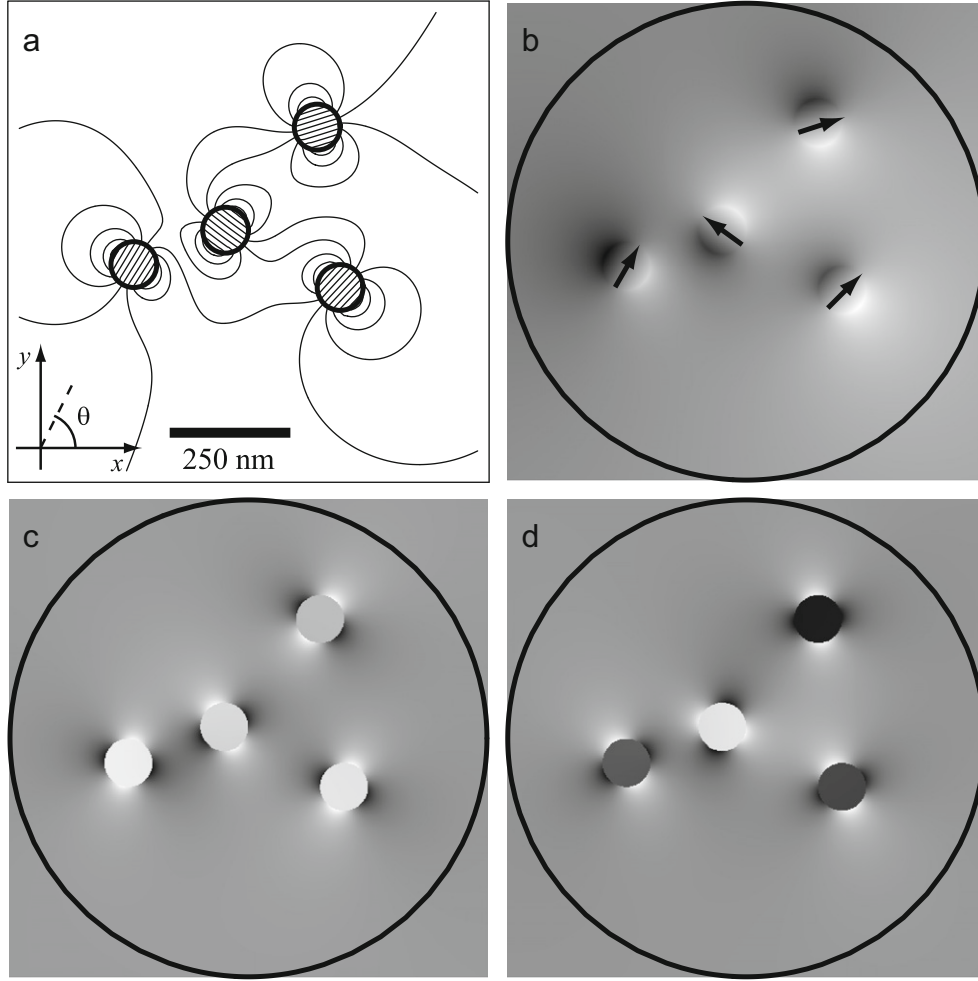


Fig. 2. Simulations of four 50-nm radius disks, each carrying 2×10^7 Bohr magnetons, magnetized in-plane at angles of 18° , 45° , 60° and 144° measured anti-clockwise from the horizontal axis: (a) magnetic projected induction map; (b) magnetic phase image, with the loop-integral contour and arrows pointing in the direction of each disk's magnetization; (c) and (d) phase gradient components, with the boundary of the circular integration region superimposed. In (a), the phase contours define a 0.25 rad shift; in (b), the grayscale covers a phase range between ± 1.13 rad; in (c) and (d), the grayscale covers a phase gradient range between ± 25 mrad/nm.

to the radius of the particle. In this example, for $R_c = 50$ nm, $|\Delta \mathbf{m}_B| = 0.44 \times 10^6 \mu_B$, or about 2%.

Similarly, if a low-frequency sinusoidal contribution to the magnetic phase is present, of the form $\beta \cos(\mathbf{k} \cdot \mathbf{r} + \gamma)$, then the measurement error is

$$\Delta \mathbf{m}_B = -\frac{2\pi\hbar\beta}{e\mu_0} J_1(kR_c) \sin(\gamma) R_c (\hat{\mathbf{z}} \times \hat{\mathbf{k}}), \quad (30)$$

where $J_1(x)$ is a Bessel function of the first kind. If the periodicity is much larger than the radius of integration, then

$$\Delta \mathbf{m}_B \sim -\frac{\pi\hbar\beta}{e\mu_0} \sin(\gamma) R_c^2 (\hat{\mathbf{z}} \times \mathbf{k}), \quad (31)$$

which is, again, quadratically proportional to R_c . For the same nanocrystal, the smallest error for $R_c = 50$ nm, $k = 10$ mrad/nm (corresponding to a periodicity of 628 nm), $\beta = 0.1$ rad and $\gamma = \pi/4$ would be $|\Delta \mathbf{m}_B| = 0.31 \times 10^6 \mu_B$.

4.3. Perturbed reference wave

When acquiring a phase image using off-axis electron holography, a magnetized object may generate a stray field that affects the reference wave, and hence the reconstructed phase, which is the difference between the “true” phase and that of the reference wave. This situation is shown schematically in Fig. 3 for

a sphere that is magnetized parallel to a biprism wire. By making use of Eq. (24), the error in the inductive moment is

$$\Delta \mathbf{m}_B = -\frac{\pi}{\mu_0} R_c^2 \mathbf{B}_p(\mathbf{d}), \quad (32)$$

where \mathbf{d} is the interference distance vector and \mathbf{B}_p is the projected induction at this position from the center of the circle of integration. For a typical interference distance of $1 \mu\text{m}$, it can be assumed that the stray field generated by a nanocrystal is dipolar. Hence, a 50 nm particle magnetized at 1 T along y (as in Fig. 3) generates a projected stray field (oriented a few degrees from $-y$) of about 80 mT nm at a distance of $1 \mu\text{m}$ along x (perpendicular to the biprism wire) from the center of the integration circle. By choosing the smallest possible circle of integration (unlike in Fig. 3), the minimal error associated with the magnetic moment measurement is $|\Delta \mathbf{m}_B| = 0.56 \times 10^5 \mu_B$, which appears to be substantially lower than errors associated with other artifacts. Note, however, that the measured orientation of $\mathbf{m}_B + \Delta \mathbf{m}_B$ may also differ from the orientation of the unperturbed \mathbf{m}_B .

4.4. Neighboring magnetic particles

Neighboring magnetic particles that are not included in the integration radius introduce perturbative effects similar to that of the reference wave described above. For two magnetic particles

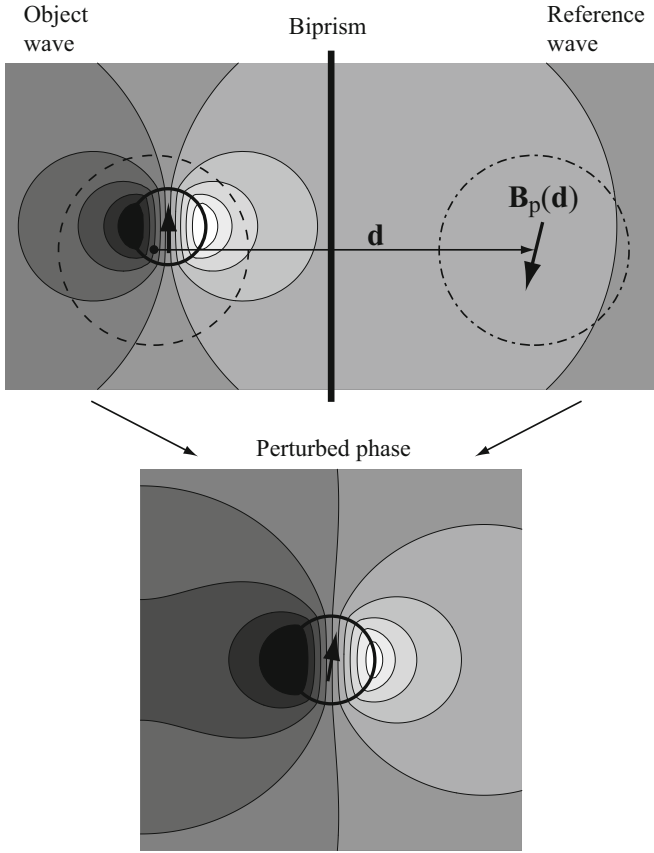


Fig. 3. Schematic diagram showing the effect of a perturbed reference wave on the magnetic induction for a sphere that is magnetized parallel to the direction of a biprism wire used to acquire an off-axis hologram. The thick circular continuous lines represent the outline of the sphere; the dashed line represents a possible off-centered circular region of integration; the dot-dashed line indicates the corresponding portion of the reference wave that effectively perturb the measurement of the magnetic moment with an error $\Delta \mathbf{m}_{\mathbf{B}}$ proportional to the projected field $\mathbf{B}_p(\mathbf{d})$ at a location established by the interference vector \mathbf{d} according to Eq. (32). The thick dot marks the integration circle center location.

such as those shown in Fig. 4, an integral performed in a circle that contains both spheres can be used to measure the sum of the two magnetic moments $\mathbf{m}_{\mathbf{B}}^{(1)} + \mathbf{m}_{\mathbf{B}}^{(2)}$. However, if a circle of radius R_1 encloses only sphere 1, then its magnetic moment will be affected by an error

$$\Delta \mathbf{m}_{\mathbf{B}}^{(1)} = \frac{\pi R_1^2}{\mu_0} \mathbf{B}_p^{(2)}(\rho_{21}), \quad (33)$$

where ρ is the vector connecting the center of sphere 2 with the center of the dashed circle in Fig. 4 (not necessarily coincident with the center of sphere 1). Similarly, measurement over a circle of radius R_2 that encloses only sphere 2 yields an error

$$\Delta \mathbf{m}_{\mathbf{B}}^{(2)} = \frac{\pi R_2^2}{\mu_0} \mathbf{B}_p^{(1)}(\rho_{12}). \quad (34)$$

If N neighboring particles are present, then each of these will contribute to the measurement error of particle j with its own projected field:

$$\Delta \mathbf{m}_{\mathbf{B}}^{(j)} = \frac{\pi R_c^2}{\mu_0} \sum_{i=1}^N \mathbf{B}_p^{(i)}(\rho_{ij}), \quad (35)$$

where ρ_{ij} is the vector connecting the center of particle i with the center of the integration circle enclosing particle j only.

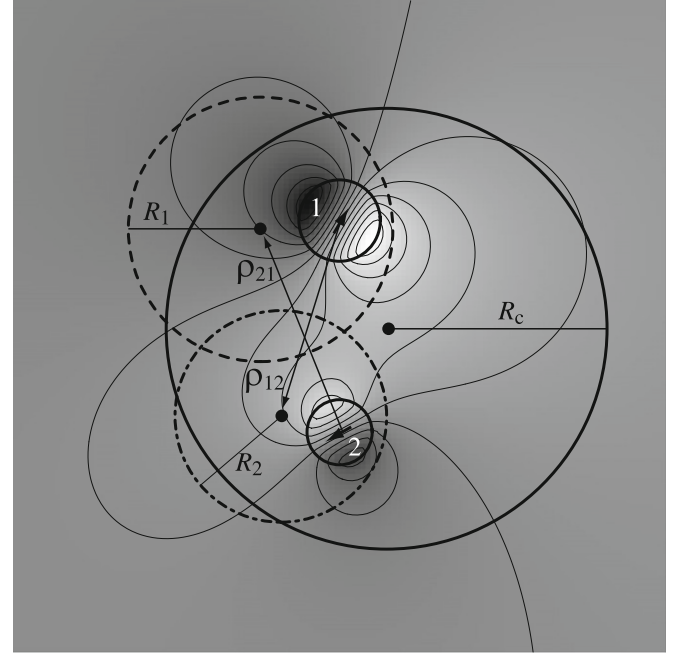


Fig. 4. Simulated phase shift for two magnetized ($M = 1$ T) spheres of radii 50 nm (1) and 40 nm (2). The magnetic moments are oriented at 60° (1) and -150° (2) off the horizontal axis. Superimposed, phase contours spaced at 0.4 radians. The larger circle of radius R_c is used to measure the sum of the two moments. The dashed circle encloses only sphere 1, and may be employed to measure its moment perturbed by the influence of the nearby sphere 2. Similarly, the dot-dashed circle enclosing only sphere 2 yields its moment perturbed by sphere 1. Perturbations are described by Eqs. (33) and (34).

4.5. Combining errors

All of the perturbations to the inductive moment described above are proportional to the area of the integration circle, suggesting that their combined effects can be considered together in the form:

$$\Delta \mathbf{m}_{\mathbf{B}}^{\text{tot}} = \frac{1}{\mu_0} \left\{ \frac{\hbar}{e} [1 - \beta \sin(\gamma)] (\hat{\mathbf{z}} \times \mathbf{k}) - \mathbf{B}_p(\mathbf{d}) + \sum_{i=1}^N \mathbf{B}_p^{(i)}(\rho_i) \right\} \pi R_c^2. \quad (36)$$

Consequently, by drawing circles of increasing radius around an object, and fitting the data with a parabolic function, the results (for each component of the inductive moment) can be extrapolated to a circle of zero radius, at which all perturbations would be expected to vanish. Repetition of the measurements for different positions of the integration loop center can then be used to improve the statistics of the measured moment further.

5. Experimental results

In order to illustrate the application of the above equations to an experimental phase image, we measure the magnetic moment of the chain of three ferrimagnetic magnetite nanocrystals shown in Fig. 1. Fig. 5 shows the magnetic contribution to the phase shift obtained by calculating half of the difference between phase images acquired with the chain of particles magnetized in opposite directions, and in addition after removing a residual linear phase ramp. Although the chain of three particles is associated with a clear step in phase, the image in Fig. 5 contains numerous additional artifacts, including loops of contrast around two of the particles (possibly due to a slight focus change between holograms or, perhaps, changes in

diffraction contrast), small changes in substrate morphology and Fresnel fringes from the edges of the biprism wire, in addition to statistical noise.

The minimum radius of the integration circle that lies outside the physical boundary of the three crystals, about 100 nm, yields a magnetic moment of $2.29 \times 10^6 \mu_B$ oriented at 136° (see Fig. 5(a)). The maximum radius that is compatible with the available field of view and centered on the same position, ~ 240 nm, yields a moment of $1.02 \times 10^6 \mu_B$ oriented at 126° (see Fig. 5(b)). By varying the radius in 1 nm increments between these values, a set of measurements for the two components of the magnetic moment that can be extrapolated quadratically to zero circle radius is obtained, as shown in Fig. 5(d).

The best-fitting values for the two moment components are $m_B^x = -(1.99 \pm 0.14) \times 10^6 \mu_B$ and $m_B^y = (1.89 \pm 0.22) \times 10^6 \mu_B$, which, together, result in a vector of modulus $(2.74 \pm 0.18) \times 10^6 \mu_B$ oriented at $(136 \pm 4)^\circ$, approximately 20% higher in modulus (but oriented similarly) than that inferred when using the circle of smallest radius alone. Error bars are estimated as the square root of the statistical variance associated to the parabolic fit of each component, and assigned to the modulus and angle according to standard error propagation theory. For the overall perturbation, i.e., the coefficient of proportionality between the integration circle area and the measurement error (the terms within brackets in Eq. (36)), we obtain in this case a projected magnetic field of about 86 mT nm oriented at about 145° .

To compare the results with what may be expected, we have estimated the radii of the three magnetic particles to be approximately (20 ± 2) nm; dividing the magnetic moment (twice the inductive moment, or $(5.5 \pm 0.4) \times 10^6 \mu_B$) by the total estimated volume of the particles $(1.0 \pm 0.2) \times 10^5 \text{ nm}^3$, we obtain an average magnetization of $(5.1 \pm 0.9) \times 10^5 \text{ A/m}$, corresponding to (0.64 ± 0.12) T. The expected magnetization of magnetite, as reported in the literature, is around 0.6 T [20], thus confirming the soundness of our approach. In this estimate, most of the rather large resulting uncertainty on the average magnetization comes from the error on the volume ($\sim 20\%$) rather than on the moment ($\sim 7\%$). If we consider the magnetization of magnetite known and equal to 0.6 T, our measurement indicates that a total volume of $(1.06 \pm 0.07) \times 10^5 \text{ nm}^3$ is magnetized, corresponding to an average radius of (20.4 ± 0.8) nm for each of the three particles in the chain.

The ratio between the average magnetization as it results from the measurement of the magnetic moment, and the saturation magnetization of the material, may be interpreted as an indication of the degree of uniformity in the magnetization state of the particle: a ratio equal to one can be obtained only when all moments are aligned (perfect uniformity), while a small ratio that approaches zero is the fingerprint of closure domains and, in general, non-uniformities. Here, the ratio is (1.1 ± 0.2) , suggesting that the elementary magnetic moments in the chain are very much aligned.

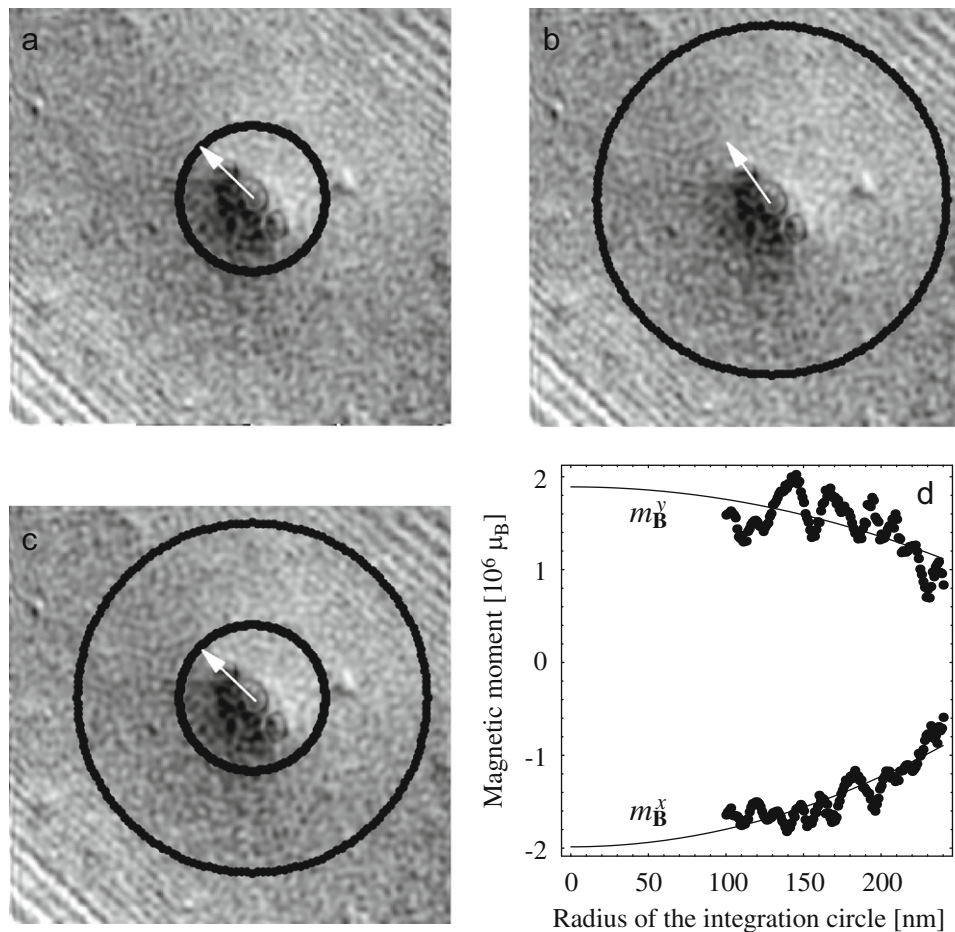


Fig. 5. (a)–(c) Magnetic contribution to the recorded phase shift corresponding to the off-axis electron hologram and magnetic induction map shown in Fig. 1. The circles and arrows show the integration radius and the direction of the resulting inductive moments for radii of: (a) 100 nm, (b) 240 nm and (c) when using integration radii between 100 and 240 nm to obtain a value for the magnetic moment extrapolated quadratically to zero integration radius. (d) Shows the parabolic fit of the two orthogonal components of the measured inductive moment (see text for details).

The possibility of measuring the moment of each of the particles in a set of structures will be discussed elsewhere.

6. Conclusions

An approach that can be used to measure the magnetic moment of a nanoparticle or nanostructure from a magnetic phase image recorded in a transmission electron microscope has been introduced mathematically. The magnetic moment can be measured by integrating, in a circle, the two components of the phase gradient associated with the structure of interest. The same value for the moment can be obtained by loop-integrating, along a circumference, the phase shift directly. In both cases the region of integration must contain the whole structure. In contrast to earlier methods suggested in the literature [13,14], the measurement scheme proposed here does not require any knowledge of the shape or assumption about the uniformity of the magnetization topography. Approaches for identifying and overcoming sources of error in such measurements have been described, and the application of the method to both simulated and experimental phase images has been presented.

The ability to obtain accurate and precise measurements of magnetic moments from local regions of specimens, which may have critical dimensions of below a few tens of nanometers, extends the capabilities of techniques such as electron holography for providing quantitative magnetic information about materials and devices with ultra-high spatial resolution. Such measurements may be extended in the future to studies of smaller magnetic nanocrystals (below 10 nm in size), to the measurement of magnetic moments in three dimensions (by analyzing phase images acquired at several different specimen tilt angles), and to analysis of phase images with an overwhelming noise component that may appear to contain little or no information. Future mathematical developments in the algorithms presented here (e.g., by making use of the information present in the mean-inner potential contribution to the

phase shift) may also lead to the ability to extract further information from recorded phase images.

Acknowledgment

We gratefully acknowledge Amy Chen for provision of the specimen.

References

- [1] A. Tonomura, *Electron Holography*, Springer, Berlin, 1993.
- [2] H. Lichte, M. Lehmann, *Rep. Prog. Phys.* 71 (2008) 016102.
- [3] M.R. Teague, *J. Opt. Soc. Am.* 73 (1983) 1434.
- [4] D. Paganin, K.A. Nugent, *Phys. Rev. Lett.* 30 (1998) 2586.
- [5] J.M. Thomas, E.T. Simpson, T. Kasama, R.E. Dunin-Borkowski, *Acc. Chem. Res.* 41 (2008) 665–674.
- [6] Y. Gao, D. Shindo, Y. Bao, *Appl. Phys. Lett.* 90 (2007) 233105.
- [7] M. Heumann, T. Uhlig, J. Zweck, *Phys. Rev. Lett.* 94 (2005) 077202.
- [8] K. Yamamoto, S.A. Majetich, M.R. McCartney, M. Sachan, S. Yamamuro, T. Hirayama, *Appl. Phys. Lett.* 93 (2008) 082502.
- [9] E. Snoeck, R.E. Dunin Borkowski, F. Dumestre, P. Renaud, C. Amiens, B. Chaudret, P. Zurcher, *Appl. Phys. Lett.* 82 (2003) 88.
- [10] J.-B. Park, G.-S. Park, I.-Y. Song, J.-S. Bae, J.-E. Lee, J.-H. Yoo, Y. Murakami, D. Shindo, *J. Electron Microsc.* 55 (2006) 17–21.
- [11] M. Ammar, M. LoBue, E. Snoeck, M. Hýtch, Y. Champion, R. Barrué, F. Mazaleyrat, *J. Magn. Magn. Mater.* 320 (2008) e716–e719.
- [12] E. Volkl, L. Allard, D.C. Joy, *Introduction to Electron Holography*, Kluwer Academic, New York, 1999.
- [13] R.E. Dunin-Borkowski, M.R. McCartney, M. Pósfai, R.B. Frankel, D.A. Bazylinski, P.R. Buseck, *Eur. J. Mineral.* 13 (2001) 671–684.
- [14] K. He, D.J. Smith, M.R. McCartney, *Appl. Phys. Lett.* 94 (2009) 172503.
- [15] G. Lai, T. Hirayama, A. Fukuhara, K. Ishizuka, T. Tanji, A. Tonomura, *J. Appl. Phys.* 75 (1994) 4593–4598.
- [16] S.J. Lade, D. Paganin, M.J. Morgan, *Opt. Commun.* 253 (2005) 392.
- [17] J.H. Hubbard, B. Burke Hubbard, *Vector Calculus, Linear Algebra, and Differential Forms: A Unified Approach*, second ed., Prentice-Hall Inc., Upper Saddle River, NJ, 2002.
- [18] J.D. Jackson, *Classical Electrodynamics*, third ed., Wiley (SEA) Pte. Ltd, Singapore, 1999.
- [19] G.B. Arfken, H.J. Weber, *Mathematical Methods for Physicists*, fifth ed., Academic Press, San Diego, CA, 2001.
- [20] D.J. Dunlop, Ö. Özdemir, *Rock Magnetism: Fundamentals and Frontiers*, Cambridge University Press, Cambridge, 1997.